Prediction of Spectral Acceleration Response Ordinates Based on PGA Attenuation

Vladimir Graizer,[a),c)] M.EERI, and Erol Kalkan,[b),c)] M.EERI

Developed herein is a new peak ground acceleration (PGA)-based predictive model for 5% damped pseudospectral acceleration (SA) ordinates of free-field horizontal component of ground motion from shallow-crustal earthquakes. The predictive model of ground motion spectral shape (i.e., normalized spectrum) is generated as a continuous function of few parameters. The proposed model eliminates the classical exhausted matrix of estimator coefficients, and provides significant ease in its implementation. It is structured on the Next Generation Attenuation (NGA) database with a number of additions from recent Californian events including 2003 San Simeon and 2004 Parkfield earthquakes. A unique feature of the model is its new functional form explicitly integrating PGA as a scaling factor. The spectral shape model is parameterized within an approximation function using moment magnitude, closest distance to the fault (fault distance) and V_{S30} (average shear-wave velocity in the upper 30 m) as independent variables. Mean values of its estimator coefficients were computed by fitting an approximation function to spectral shape of each record using robust nonlinear optimization. Proposed spectral shape model is independent of the PGA attenuation, allowing utilization of various PGA attenuation relations to estimate the response spectrum of earthquake recordings. [DOI: 10.1193/1.3043904]

INTRODUCTION

Since it was first introduced by Biot (1933) and later conveyed to engineering applications by Housner (1959) and Newmark et al. (1973), the ground motion response spectrum has often been utilized for purposes of recognizing the significant characteristics of accelerograms and evaluating the response of structures to earthquake ground shaking. Due to inherent theoretical simplicity and ease in its computations, the response spectrum concept has long become the standard tool of structural design and performance assessment. Mainly for this reason, prediction of response spectrum ordinates using attenuation relationships became the vital ingredient of probabilistic and deterministic seismic hazard analyses for site-specific evaluations, and seismic hazard mapping and design spectrum development for building code applications.

Accumulation of strong motion data over the last two decades has stimulated devel-

[a)] U.S. Nuclear Regulatory Commission, vxg1@nrc.gov
[b)] U.S. Geological Survey, kalkan76@msn.com
[c)] Authorship order is alphabetical

Earthquake Spectra, Volume 25, No. 1, pages 39–69, February 2009;

opment of a number of different response spectral attenuation relationships. Predictive equations of Abrahamson and Silva (1997), Boore et al. (1997), Campbell (1997), and Sadigh et al. (1997) have found widespread applications in earthquake engineering. In parallel, many researchers in Europe and Asia developed their own models to predict vernacular spectral response ordinates; the recent work by Ambraseys et al. (1996) for Europe, Sabetta and Pugliese (1996) for Italy, Theodulidis and Papazachos (1994) for Greece, Gülkan and Kalkan (2002) and later Kalkan and Gülkan (2004a, b) for Turkey, Fukushima et al. (2003) for West Eurasia, and Kanno et al. (2006) for Japan are among the others. A comprehensive summary of ground motion prediction models is reported in Douglas (2001, 2002).

In all these studies, empirical expressions and their estimator coefficients were computed through regression conducted independently at each spectral period. In other words, depending upon the period range considered, regressions (single- or multi-stage) were repeated as many times as the number of spectral periods covered, and transitions between periods are assumed to be linear. In many studies, period range considered is logarithmically spaced, meaning that more regression points are located at higher frequencies. Some developers (e.g., Abrahamson and Silva 1997, Boore et al. 1997, Campbell 1997) opted to smooth out their estimator coefficients to eliminate sudden peaks and troughs in their predictions. Regardless of the smoothing process, the final product of response spectral attenuation has always been an exhausted matrix of estimator coefficients.

When the table of estimator coefficients is closely examined (for instance, that of Boore et al. 1997), it can be observed that variations of some coefficients against spectral period are marginal or none (i.e., well-constrained), while the variations of some other coefficients are more volatile. If we assume that the empirical expression proposed is statistically robust and has the ability to represent the intricate physical attenuation of seismic radiation (at least approximately), the variability of estimator coefficients between different periods should be correlated (up to a certain extent) to independent parameter(s) of prediction, e.g., magnitude, distance, V_{S30}.

Let us assume that a given empirical equation has sufficient robustness, then its matrix of estimator coefficients can be possibly represented by a series of functions, and these functions may be integrated with the core attenuation expression. Each function in this case characterizes certain spectral variability with respect to its corresponding independent parameter(s). Eventually this approach should lead to a parameterization of highly variable ground motion spectral shape using a single continuous function of period, and eliminate the exhausted estimator coefficient matrix entirely. Based on this conceptual approach, developed herein is a new PGA-based predictive model for a 5% damped pseudospectral acceleration ordinates of free-field horizontal component of ground motions from shallow-crustal earthquakes. A new methodology is used here to construct the empirical model of spectral shape (i.e., SA/PGA) using a continuous function of few independent parameters. The parameters of the model are obtained by individually fitting an approximation function to the spectral shape of earthquake records using robust nonlinear optimization.

In the proposed model, spectral shape is parameterized for three independent variables—magnitude, fault distance, and V_{S30}. The final response spectrum of an accelerogram is obtained by anchoring its predictive spectral shape to PGA. PGA can be estimated explicitly from any attenuation relation preferred, or recorded PGA can be used directly. In a number of cases, when low-amplitude accelerations were recorded by analog-type film instruments, the records have never been digitized, and only PGA data was made available (e.g., San Simeon earthquake recorded by analog instruments at the Parkfield array). In such cases, our model allows estimating response spectrum based on actual PGA, magnitude, distance, and V_{S30}. This versatile feature also allows the user to utilize different PGA attenuation relations to estimate the ground motion response spectrum. In this study, in addition to the actual PGA data, we used our recent PGA attenuation relations (Graizer and Kalkan 2007) referred as "GK07-PGA." The proposed SA model can also be used for developing ShakeMaps (Wald et al. 1999a, b) for spectral ordinates in cases when only PGA, magnitude and distance are known input parameters.

Our spectral shape model is set on the main shocks from the NGA database (Power et al. 2006) with a number of additions mainly from recent Californian earthquakes including 2003 San Simeon and 2004 Parkfield events. All the earthquakes in database occurred in the shallow-crustal tectonic regimes (those for which the fault rupture lies mainly above a depth of 20 km) considered to be similar to that of California.

STRONG-MOTION DATABASE

A database of 1,825 strong motion records from 40 earthquakes worldwide has been created as the extended version of NGA database. Our database includes additional events or the events in the NGA dataset with additional stations, those are the 1994 Northridge, 2002 Big Bear City, 2003 San Simeon, 2004 Parkfield, 2005 Anza and Yucaipa earthquakes. Only the records from main shocks were used. The data from aftershocks were intentionally excluded because of possible change in soil condition of recording sites (especially for sites with low V_{S30}) in the aftermath of strong ground shaking. Such variations in local geological conditions were observed for instance during the 1999 earthquakes in Turkey (Safak et al. 2000, Bakir et al. 2002). In addition, the spectral ordinates at 5% of critical damping were kept in the range of 0.01 sec to 5.0 sec (total of 95 logarithmically spaced periods); spectral periods higher than 5.0 sec were not included since 5.0 sec is the long-period cutoff for most of the processed ground motion records. Most of the records from Loma Prieta, Whittier Narrows, Northridge, and even Landers earthquakes were originally filtered with the long-period cutoff of 5.0 sec or lower. Since majority of the California strong-motion data before 1994 were recorded by SMA-1 (film) instruments requiring digitization of the records, these records usually did not have high enough dynamic range to allow processing them with longer period cutoff filters. This situation has changed after the 1994 Northridge earthquake when many new digital instruments were deployed and replacement of old film recorders became more widespread as a result of TriNet seismological instrumentation project in southern California (Mori et al. 1999) and its later expansion to northern California under the California Integrated Seismic Network (CISN).

Table 1 presents all the events in our database with their relevant information on moment magnitude (M), focal depth, epicenter coordinates, distance range, and faulting mechanism. Also listed is the breakdown of record numbers used from each event. Of the total 1,825 records, 1,144 records are from reverse fault, 668 from strike-slip fault, and 13 are from normal fault events. The distributions of earthquake data with respect to moment magnitude and PGA plotted against fault distance are shown in Figure 1. As seen, the compiled dataset becomes more complete with additions to the existing NGA database not only at farther distances but also in the near-field region; it is also more inclusive in terms of magnitude range covered. The current set includes data recorded within 250 km of the earthquake faults from events in the magnitude range of 4.9 to 7.9. The latest entries are the Anza and Yucaipa earthquakes of 12 June and 16 June 2005, respectively. Figure 2 plots the distribution of earthquake data with respect to V_{S30}, also shown is the NEHRP site categories.

EVALUATION OF RESPONSE SPECTRAL SHAPE

The creation of a response spectrum shape function that matches reasonably a given response spectrum when it is anchored to PGA requires close examination of individual and average spectral shapes obtained from many recordings of varying magnitudes, distances, and site conditions. Prior to that, response spectral acceleration of each record in our database is first smoothed by using four-point moving-average method to minimize rough fluctuations; each smooth spectrum is then normalized by PGA. This later process warrants that spectral shapes converge to unity at the period of 0.01 sec.

Our objective is to investigate the characteristics of spectral shape, and describe them in terms of the following *shape parameters*: (1) peak intensity, (2) predominant (peak) period, and (3) width (i.e., spectral wideness=area under the spectral shape) with respect to following independent parameters: (a) magnitude, (b) distance, and (c) V_{S30}. Therefore, the problem that needs to be solved gains an orthogonal characteristic having 3×3 matrixes of correlations between independent parameters and *shape parameters*. Deciphering such a complex system of correlations calls for thorough analyses of the data by creating various bins, averaging them, and finally, isolating the effects of each independent parameter in a systematic way. In the following, the dependence of each *shape parameter* on independent parameters is demonstrated first using the data from major events. Their mathematical representations are given later in the section devoted to nonlinear optimization.

MAGNITUDE DEPENDENCE

In order to find the degree of magnitude influence on response spectral shape, average spectral shapes of earthquakes ranging from magnitude 4.9 to 7.9 are plotted in Figure 3. As shown, the spectral peak gradually shifts from ~0.15 sec for the lowest magnitude earthquake (M4.9) to ~0.5 sec for the largest events (M7.6 to 7.9). Maximum amplitudes of the average spectral shape are relatively stable varying from 2.3 to 2.6, with higher amplitudes at smaller magnitudes. In general, events with larger magnitude yield wider spectra. These observations are consistent with all empirical and theoretical models of Fourier and response spectra.

Table 1. List of events used in development of Graizer-Kalkan prediction model for 5% damped response spectral acceleration ordinates

No	Event	Date	M_w	Style of Faulting	Depth (km)	Epicenter Coordinates		Number of Data	Distance Range (km)	Data Source[b]
						Lattidute	Longitude			
1	ANZA[a]	2005	5.2	Strike-Slip	14.2	33.529	−116.573	102	18.8–168.9	2
2	BIG BEAR CITY[a]	2003	5.2	Strike-Slip	6.3	34.310	−116.848	91	8.0–150.8	1
3	BISHOP (RND. VAL.)	1984	5.8	Strike-Slip	9.0	37.460	−118.590	1	21.9	1
4	BORREGO MNT.	1968	6.6	Strike-Slip	8.0	33.190	−116.142	5	45.7–222.4	1
5	CHALFANT VALLEY	1986	5.8	Strike-Slip	6.7	37.577	−118.449	5	6.4–24.5	1
6	CHI-CHI (TAIWAN)[a]	1999	7.6	Reverse	16.0	23.860	120.800	419	0.3–172.2	1
7	COALINGA-01	1983	6.4	Reverse	4.6	36.233	−120.310	46	8.4–55.8	1
8	COALINGA-05	1983	5.8	Reverse	7.4	36.241	48.491	11	4.6–16.2	1
9	COYOTE LAKE	1979	5.7	Strike-Slip	9.6	37.085	−121.505	10	3.1–33.8	1
10	DENALI (ALASKA)[a]	2002	7.9	Strike-Slip	4.9	63.538	−147.444	24	2.7–275.9	1
11	DÜZCE (TURKEY)[a]	1999	7.2	Strike-Slip	10.0	40.740	31.210	23	0.2–188.7	2
12	FRIULI (ITALY)	1976	6.5	Reverse	5.1	46.345	13.240	5	15.8–102.2	1
13	GULF OF CALIFORNIA	2001	5.7	Strike-Slip	10.0	32.037	−114.906	12	76.7–134.1	1
14	HECTOR MINE[a]	1999	7.1	Strike-Slip	5.0	34.574	−116.291	53	52.3–217.7	2
15	IMPERIAL VALLEY[a]	1979	6.5	Strike-Slip	10.0	32.644	−115.309	33	0.1–50.1	1
16	KOCAELI (TURKEY)[a]	1999	7.4	Strike-Slip	15.0	40.727	29.990	31	3.2–349.6	2
17	LANDERS[a]	1992	7.3	Strike-Slip	7.0	34.200	−116.430	69	2.2–190.1	1
18	LAZIO-ABRUZZO (ITALY)	1984	5.8	Normal	14.0	41.710	13.902	5	18.9–51.3	1
19	LITTLE SKUL MTN. (NEVADA)	1992	5.7	Normal	12.0	36.720	−116.286	8	16.1–100.2	1
20	LIVERMORE	1980	5.8	Strike-Slip	12.0	37.855	−121.816	7	16.7–56.1	1
21	LOMA PRIETA[a]	1989	6.9	Reverse/Strike	17.5	37.041	−121.883	82	3.9–117.1	1
22	MAMMOTH LAKES-02	1980	5.7	Strike-Slip	14.0	37.628	−118.927	3	9.1–16.9	1
23	MAMMOTH LAKES-03	1980	5.9	Strike-Slip	16.0	37.561	−118.831	4	5.9–11.5	1
24	MAMMOTH LAKES-04	1980	5.7	Strike-Slip	5.0	37.625	−118.859	4	2.8–14.2	1
25	MAMMOTH LAKES-06	1980	5.9	Strike-Slip	14.0	37.506	−118.856	5	12.0–46.5	1
26	MANJIL (IRAN)	1990	7.4	Strike-Slip	19.0	36.810	49.353	7	12.6–174.6	1
27	MORGAN HILL	1984	6.2	Strike-Slip	8.5	37.306	−121.695	28	0.5–70.9	1
28	NORTH PALM SPRINGS	1986	6.1	Strike-Slip/Thrust	11.0	34.000	−116.612	32	8.6–268.0	1

Table 1. (cont.)

No	Event	Date	M_w	Style of Faulting	Depth (km)	Epicenter Coordinates		Number of Data	Distance Range (km)	Data Source[b]
						Lattidute	Longitude			
29	NORTHRIDGE[a]	1994	6.7	Reverse	17.5	34.206	−118.554	159	5.2–147.6	2
30	PARKFIELD	1966	6.2	Strike-Slip	10.0	35.955	−120.498	6	6.3–63.3	2
31	PARKFIELD[a]	2004	6.0	Strike-Slip	8.8	35.819	−120.364	77	0.3–164.5	2
32	SAN FERNANDO[a]	1971	6.6	Reverse	13.0	34.440	−118.410	44	1.8–218.8	1
33	SAN SIMEON[a]	2002	6.5	Reverse	7.1	35.702	−121.108	51	12.4–317.8	1
34	SANTA BARBARA	1978	5.9	Thrust	12.7	34.399	−119.681	2	12.2–27.4	1
35	SIERRA MADRE	1991	5.6	Reverse	12.0	34.259	−118.001	9	10.4–48.2	1
36	SUPERSTITION HILLS-02	1987	6.5	Strike-Slip	9.0	33.022	−115.831	11	1.0–27.0	1
37	TAIWAN, SMART(5)	1981	5.9	Reverse	11.1	24.429	121.896	7	28.7–32.0	1
38	WHITTIER NARROWS[a]	1987	6.0	Reverse	14.6	34.049	−118.081	116	14.5–103.9	1
39	YOUNTVILLE	2000	5.0	Strike-Slip	10.1	38.379	−122.413	25	9.9–95.7	1
40	YUCAIPA[a]	2005	4.9	Reverse	11.6	34.058	−117.011	193	2.9–128.9	2
								Total=1825		

[a] Major event used for constraining sub-functions of spectral shape model
[b] Data complied by: (1) NGA; (2) E. Kalkan & V. Graizer

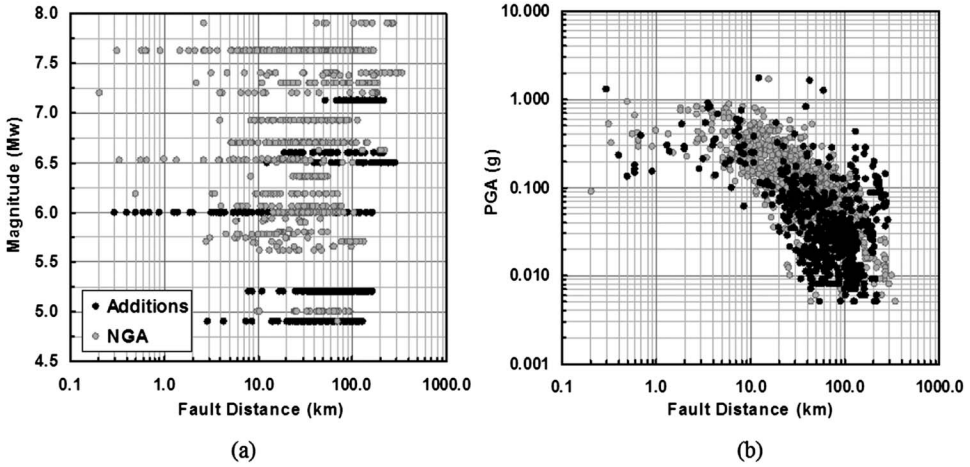

Figure 1. Earthquake data distribution with respect to (a) moment magnitude and (b) PGA of records in the database.

DISTANCE DEPENDENCE

As reported in previous studies (e.g., Abrahamson and Silva 1997), predominant period shifts to higher values with increase in distance from the fault for a given earthquake. Figure 4 depicts such a distance dependence on the spectral shape whereby variations of maximum period for different distance bins are plotted for the 1999 M7.6 Chi-

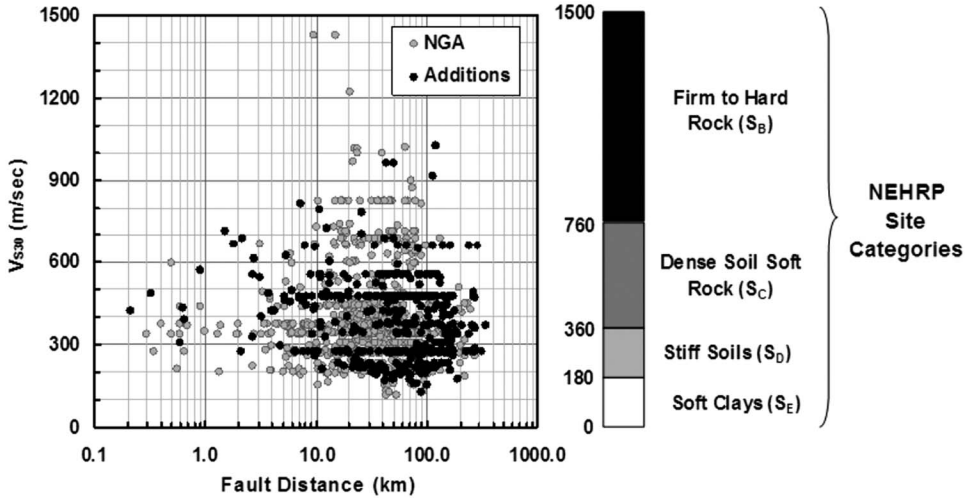

Figure 2. Earthquake data distribution with respect to V_{S30} and its comparison with NEHRP site categories.

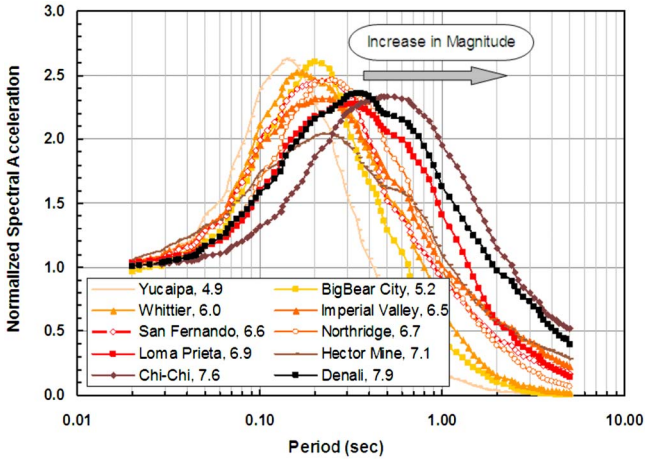

Figure 3. Comparison of average spectral shape of earthquakes in magnitude range of 4.9 to 7.9 (*increase in magnitude shifts the predominant period to higher values*).

Chi earthquake (bins with a very small number of records were not considered). For this particular event, predominant period shifts from about 0.35 sec at the closest distances (0 to 20 km bin) to 1.2 sec at farthest fault distances (120 to 140 km bin). Similar observations are valid for the other major events investigated.

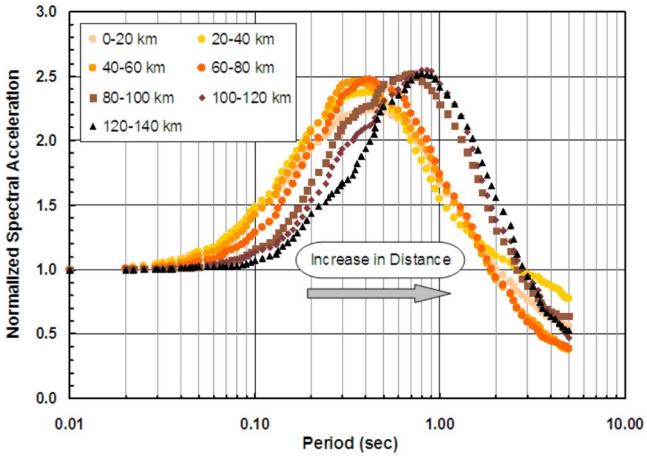

Figure 4. Shift of predominant period of average spectral shape to higher values with increase in average distance within each 20 km distance bin (*data values correspond to the 1999 M7.6 Chi-Chi earthquake*).

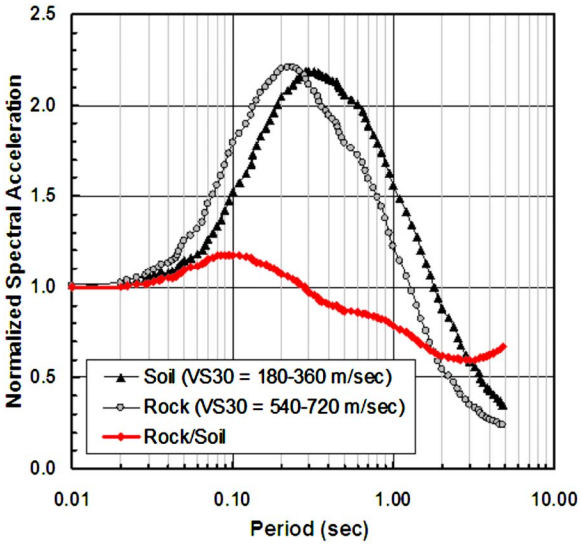

Figure 5. Comparison of average "rock" and "soil" spectral shapes and their transfer function (rock/soil).

SOIL CONDITION DEPENDENCE

In addition to magnitude and distance dependence, spectral shape also depends on site conditions. Predominant period of spectral shape from a rock site is generally lower than that of a soil site. This tendency is shown in Figure 5, which compares the average spectral shape in V_{S30} bin of 180 to 360 m/sec with that of 540 to 720 m/sec. At short periods, spectral shape of average rock site remains above that of average soft-soil, while the reverse takes place beyond the spectral period of 0.3 sec. Unlike predominant period shifting to higher values with reduction in V_{S30}, peak intensity of spectral shapes remains similar.

BASIN EFFECT

A number of studies provide convincing examples of significant impacts of deep sedimentary basin on seismic wave field at distances of about 50 km and more (e.g., Lee et al. 1995, Joyner 2000, Field 2000, Frankel et al. 2001). For example, during the Hector Mine earthquake, average PGA had almost no attenuation at the distances of 130 to 230 km from the fault due to dominant basin waves in the Los Angeles, San Bernardino, and Long Beach basins (Graizer et al. 2002). Basin effects exhibit shaking level amplification and also may result in more complex spectral shape with concurrent multiple peaks at lower (0.3 to 0.6 sec) and higher spectral periods (5.0 to 7.0 sec). The first spectral peak in such cases is associated with earthquake source effect, and the second one is the result of deep basin excited by long period seismic waves.

DIRECTIVITY EFFECT

Theoretical and experimental seismological studies have shown that directivity and type (unilateral or bilateral) of earthquake rupture propagation modify frequency content of seismic radiation. Rupture directivity essentially enriches the spatial variations in ground motion amplitude and duration in the near-field zone. The rupture propagation models for specific earthquakes developed by different authors may vary significantly. Empirical results of Somerville et al. (1997) and Rowshandel (2006) show that directivity effects on spectral response may be effective at periods longer than 0.6 sec. Similar to the NGA relations (Abrahamson and Silva 2008, Campbell and Bozorgnia 2008, Boore and Atkinson 2008, Chiou and Youngs 2008, Idriss 2008) the influences of directivity effect have not been incorporated in our predictive model yet.

APPROXIMATION FUNCTION FOR SPECTRAL SHAPE

It looks attractive to find a mathematical function describing physical model of the response spectrum. Udwadia and Trifunac (1973) demonstrates the correlation between Fourier and response spectra through a concept of damped Fourier spectra. This approach shows that the correlation is complex and does not result in approximation of response spectrum with certain mathematical functions. Rather than seeking a theoretical approach, we opted to use an empirical one. Our procedure to formalize the spectral shape commences with an approximation function. This function should reasonably replicate the response spectral shape while providing sufficient versatility to accommodate the complex variability due to nonstationary nature of earthquake ground motions. We first started with a well-known transfer function of a single-degree-of-freedom (SDF) oscillator by replacing the frequency (f) parameter with period (T):

$$F_0(T) = [(1 - (T/T_0)^2)^2 + 4D_0^2 \cdot (T/T_0)^2]^{-1/2} \tag{1}$$

This tailored function $[F_0(T)]$ remains flat at short periods, attenuates proportional to T^{-2} at long periods and has a resonance around the natural period, T_0 for damping ratios, $D_0 < 0.6$. Comparisons with actual data show that such an approximation function itself does not produce acceptable match of a real spectral shape especially at low period region. Summation of a modified lognormal probability density function $[F_1(T)]$ with altered SDF oscillator transfer function $[F_2(T)]$ eventually provides the desired shape and also enough flexibility to fit into wide range of spectral shape of real recordings. Each one of these functions simulates certain spectral behavior, for that reason their combination $[F(T) = F_1(T) + F_2(T)]$ results in a powerful predictive model.

Note that $F_1(T)$ is a modified log-normal probability density function (PDF), and can be expressed as

$$F_1(T/M,R,V_{S30}) = I(M,R)e^{-\frac{1}{2}\left(\frac{\ln(T) + \mu(M,R,V_{S30})}{S(M,R)}\right)^2} \tag{2}$$

where T is the spectral period, R is the closest distance to the fault. $I(M,R)$ is the intensity subfunction which is set to adjust the shape parameter-1 (peak spectral intensity). $I(M,R)$ is a function of magnitude and distance only. $\mu(M,R,V_{S30})$ is set to model the

location of predominant period (i.e., *shape parameter*-2) and depends upon magnitude, distance and site geology. Width of bell-shape (spectral wideness) defined previously as *shape parameter*-3 is adjusted by $S(M,R)$. Note that we found relatively strong V_{S30} dependence on μ unlike I and S in which magnitude (M) and distance (R) appeared to be the main influential parameters.

Equation 2 is asymptotic to zero at short and long periods. Therefore, $F_1(T)$ is not sufficient itself to represent the spectral shape which starts at unity, and shows decay after predominant period with tendency of being asymptotic to zero at long periods. However, $F_1(T)$ allows us to adjust the intensity, predominant period, and also to narrow down or widen the bell-shape in the spectral shape. All of the above-mentioned features are important to achieve a best fit.

The second function $F_2(T)$ is the modified SDF oscillator transfer function. Its original form constitutes the core of our PGA prediction model (Graizer and Kalkan 2007). With slight modification from Equation 1, the following functional form is obtained:

$$F_2(T) = \left[(1-(T/T_{sp,0})^{\zeta})^2 + 4D_{sp}^2 \cdot (T/T_{sp,0})^{\zeta}\right]^{-1/2} \tag{3}$$

where $T_{sp,0}$ and D_{sp} ("*sp*" stands for spectrum) are the shape parameters controlling respectively the mid of transition region affecting shape parameter-2 (predominant period), and intensity of peak and also post-peak decay. Since $F_2(T)$ is used in combination with $F_1(T)$, there is no need for introducing additional bump (amplification) at a period of $T_{sp,0}$. Consequently, D_{sp} is set as 0.75 in Equation 3. Note that lower D_{sp} would result in bump associated with Equation 3 around the period $T_{sp,0}$.

The function $F_2(T)$ has all essential features to accommodate the missing parts in spectral shape fit. By summing $F_1(T)$ and $F_2(T)$, an approximation function of spectral shape, denoted as SA_{norm} ("*norm*" stands for normalized), is obtained as

$$SA_{norm}(T/M,R,V_{S30}) = I(M,R)e^{-\frac{1}{2}\left(\frac{\ln(T)+\mu(M,R,V_{S30})}{S(M,R)}\right)^2} + \left[(1-(T/T_{sp,0})^{\zeta})^2 + 4D_{sp}^2(T/T_{sp,0})^{\zeta}\right]^{-1/2} \tag{4}$$

where $T_{sp,0}=f(M,R,V_{S30})$ is a function of magnitude, distance and site condition. In Figure 6a, both $F_1(T)$ and $F_2(T)$ and their summation (i.e., Equation 4) are plotted against the average spectral shape from Chi-Chi earthquake. Parameter "ζ" controls the slope of spectral shape decay at long periods. Equation 4 with $\zeta=1.0$ results in good match up to period of about 3 seconds, beyond that there is a notable misfit, and average curve is overestimated. This tendency, also observed for other events, is corrected by increasing the order of ζ to 1.5. Faster decay of $\zeta=2.0$ seems to produce underestimation at long periods (Figure 6b). Estimating the slope of attenuation of the response spectrum at long periods may require further studies and a more uniformly (from the standpoint of long-period filter cutoff) processed dataset because many strong-motion records have been processed with long-period cutoff at 3 to 5 seconds. Corrected records in the PEER-NGA strong-motion database were processed using 5-pole Butterworth filter at the long-period end and 4-pole Butterworth filter at the short-period end. It translates into influ-

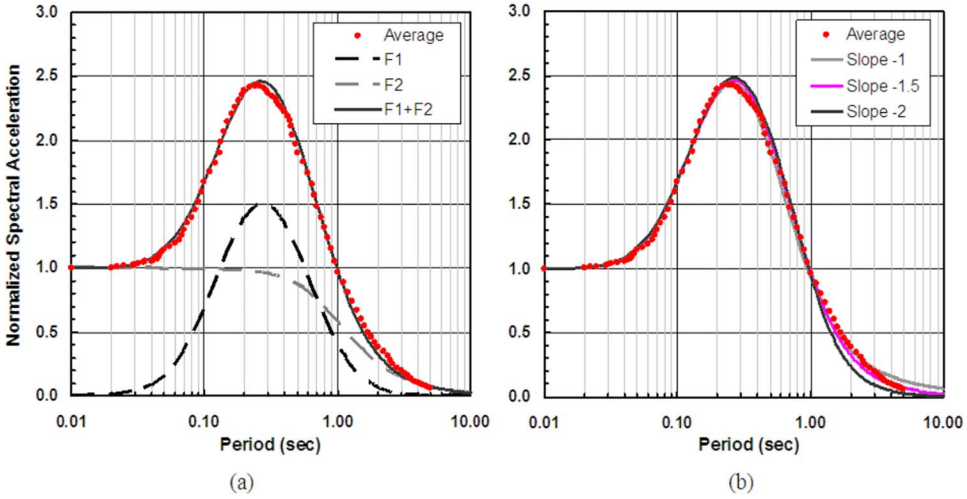

Figure 6. Approximation function fit to average spectral shape of the 1999 M7.6 Chi-Chi earthquake (*slope of approximation function shown in left-panel is* ζ=−1.5).

ence on the long-period region of the response spectra by the data processing procedure.

As shown in Figure 6, average spectrum has different decay before and after its predominant (peak) period. By combining $F_1(T)$ with $F_2(T)$, such difference in slope can be adequately simulated. Function $F_2(T)$ constrains the approximation function to unity at low-period end, and also controls decay at long-periods. $\mu(M,R,V_{S30})$ and $T_{sp,0}(M,R,V_{S30})$ in Equation 4 collectively identify the location of predominant peak, which is one of the most important shape parameter for spectral shape fit. Likewise, $S(M,R)$ and D_{sp} describe the wideness of the bell-shape in combination. It is worth emphasizing that Equation 4 is a continuous function of spectral period, T; therefore it is very efficient to be used in nonlinear optimization.

Silva et al. (2001) developed an approach to fit response spectral shapes to a specific functional form with only two variables (magnitude and distance). According to the authors, the equation was not based on physical model but was designed to fit general characteristics of the spectral shape. The above-mentioned equation was a combination of the two functions: a function inverse to hyperbolic cosine and an exponential function divided per power function. The authors only used this approximation in limited applications for nuclear industry, without trying to extend it for use in ground motion attenuation modeling. We were not aware of this publication at the time of the preparation of the manuscript, and our approach differs significantly from the approach of Silva et al. (2001).

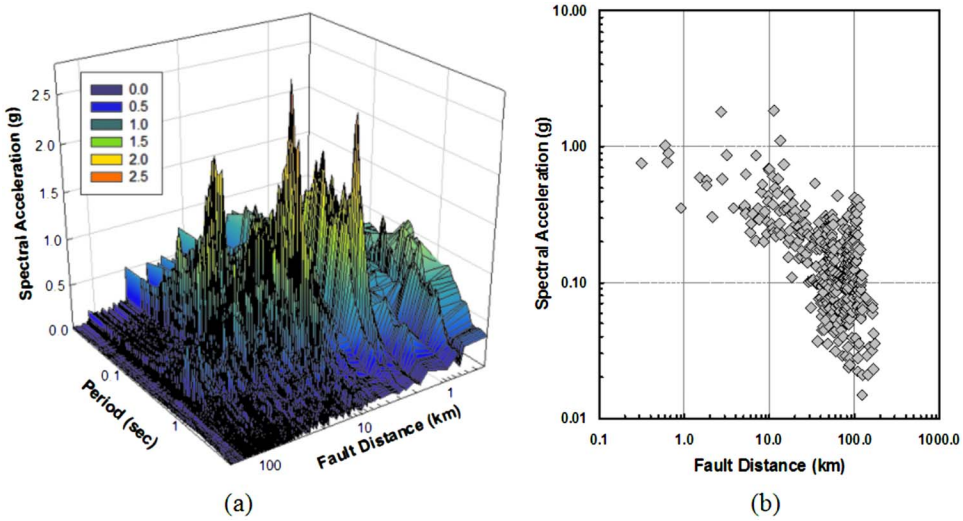

Figure 7. Comparison of spectral attenuation surface with attenuation of spectral acceleration at 1.0 sec. (*spectral data is plotted in increasing distance order and corresponds to the 1999 M7.6 Chi-Chi earthquake, Chi-Chi data is selected because it has the largest number of records measured*).

NONLINEAR OPTIMIZATION OF SPECTRAL SHAPE

PROBLEM DESCRIPTION

In a conventional approach of developing a ground motion prediction model, an empirical expression is fitted into response spectral data individually at each period, and corresponding estimator coefficients are computed using standard least square method. This type of regression is essentially limited to a number of data points and corresponding spectral acceleration values in two-dimensional (2-D) space. In contrast, when we attempt to find a continuous attenuation function applicable for all spectral periods (0 to 5 sec), discrete utilization of spectral data from the entire period range and systematic evaluation of such a complex system are required. Therefore, the problem turns into more intricate three-dimensional (3-D) surface fitting, where spectral acceleration, period, and number of records constitute the three orthogonal axes. Figure 7 compares such a spectral attenuation surface plotted in increasing distance order with the attenuation of spectral acceleration at 1.0 sec for the Chi-Chi earthquake. Apparently, the empirical predictive expression (i.e., simple attenuation curve) can be easily fitted to the 2-D distribution of data points; however, this approach requires repetition of same regression process at each spectral period to estimate the entire spectrum. In contrast, our aim is to fit into the 3-D attenuation surface using a single continuous equation. Its estimator coefficients are independent of spectral period, thereby a long table of estimator coefficients can be eliminated.

SOLUTION STRATEGY

Although there are numerous methods to conduct direct surface fitting, complex physical attenuation process and associated roughness of response spectral surface (e.g., Figure 7a) require close examination of spectral shapes and careful identification of their weak and strong parametric dependences. Therefore, in lieu of a blind surface fitting, our solution strategy encompasses sequential nonlinear optimization. Three major steps of the solution strategy we followed are:

1. Individual fitting to each smoothed spectral shape of records in the database using an approximation function via nonlinear optimization
2. Examining the variability of estimator coefficients via their probability density functions (PDFs) and finding their dependence with respect to independent variables. This step requires partitioning of estimator coefficients by magnitude, distance and V_{S30} bins, and also constraining and limiting the characteristics of "shape parameters" via subfunctions (I, μ, $T_{sp,0}$ and S).
3. Repeating Steps 1 and 2 as deemed necessary to achieve the best estimator coefficients with least standard errors

Details of each step and their implementation are explained in the following subsections.

Step 1: Nonlinear Optimization and Individual Spectral Shape Fitting

Figure 7a exemplifies the variation of response spectra of a given earthquake with distance. In order to approximately fit to such highly scattered data points, an equation of known form is needed. As mentioned, Equation 4 is set previously as our approximation function for describing the generic spectral shape of earthquake records. Initially, its subfunctions for shape parameters and more importantly their dependence on magnitude, distance and V_{S30} are all unknown. Therefore, $I(M,R)$, $\mu(M,R,V_{S30})$, $S(M,R)$ and $T_{sp,0}(M,R,V_{S30})$ are first treated as single variables—simply as I, μ, S and $T_{sp,0}$. Their functional forms are constructed later in Step 2 after obtaining the statistical variation of each of them with respect to independent parameters. Notably, I, μ, S, $T_{sp,0}$ are all dependent parameters and their statistical distributions are computed by fitting Equation 4 to smoothed spectral shape of each record via nonlinear optimization. The optimization algorithm utilized for that purpose (i.e., MATLAB intrinsic function of "fminsearch") relies on Nelder-Mead method of nonlinear minimization which finds the minimum of a scalar function of several variables, starting at an initial estimate (see Wilson et al. 2003 for details of Nelder-Mead method and its MATLAB implementation). Commencing with realistic initial estimates of dependent variables is the key in reaching the optimal solutions while avoiding bifurcations and/or nonconvergence conditions. Accordingly, Equation 4 is first manually fitted to average spectral shape of individual earthquakes, and then the means of each best-fit parameter are taken as initial estimate values to start. It is in this manual phase that D_{sp} and ζ are constrained respectively as 0.75 and 1.5. These two values yield the best fit of approximation to the average spectral shapes.

Figure 8 exemplifies four cases out of 1,825 records in our database, where Equation 4 is fitted to the spectral shape of Sylmar Olive View Hospital and Rinaldi Receiver Sta-

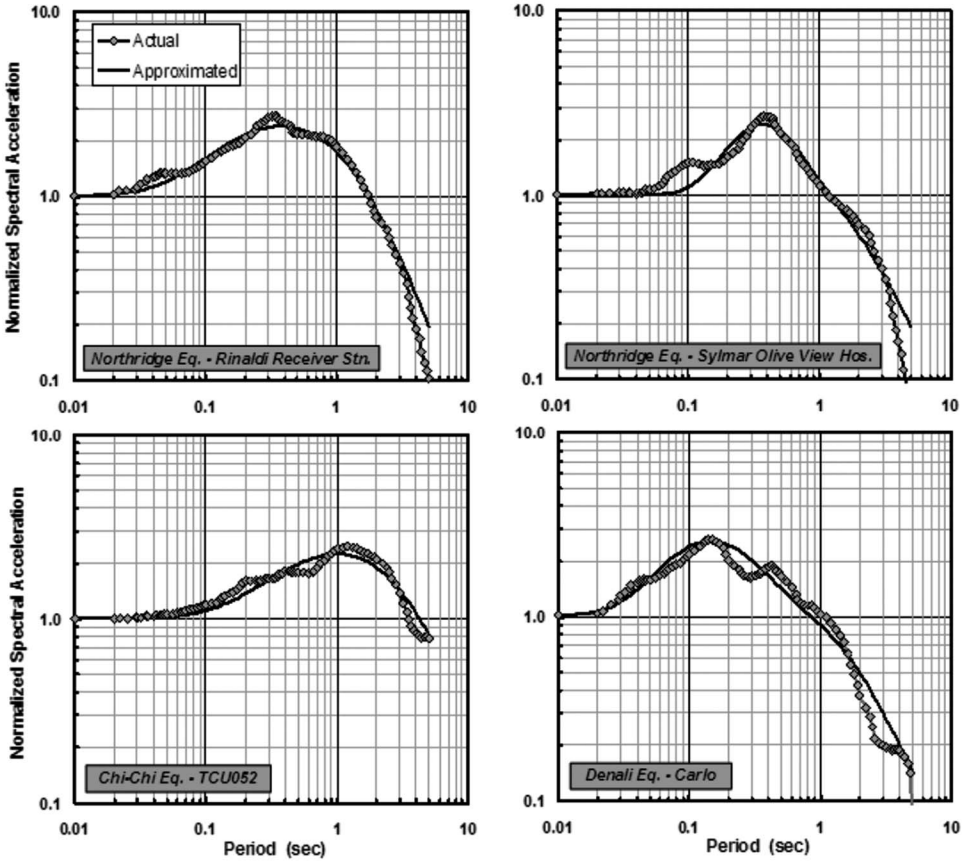

Figure 8. Individual fitting of approximation function to spectral shapes of selected Northridge (Slymar Olive View Hospital and Rinaldi Receiver Stn.), Chi-Chi (TCU052), and Denali (Carlo) records.

tion records of the Northridge, TCU052 record of the Chi-Chi and Carlo record of the Denali earthquake. Selected Northridge records have dominant periods in the mid-period range. The TCU052 record's spectral shape is an example for long period dominant record, and the Carlo record has strong spectral content at short periods. As shown, the approximation function plotted has sufficient versatility to fit into very different spectral shapes. It should also be noted that each window is independent from the other; therefore, nonlinear fit results in different estimator coefficients. These comparisons (and with many others not shown here) collectively indicate that all the shape parameters described earlier (predominant period, peak intensity, post-peak decay, and wideness of spectral shape) are represented reasonably using the approximation function given in Equation 4.

Step 2: Correlating Dependent Parameters with M, R and V_{S30}

By fitting Equation 4 to 1,825 smooth spectral shapes separately in Step 1, the PDFs of all dependent parameters are obtained. As expected, there is a significant variation for each dependent parameter, indicating the large variability in response spectral shape of actual recordings. For μ and $T_{sp,0}$ (two parameters describing the predominant period of spectral shape), the variability is even more dramatic as compared to S (shape parameter for wideness) and I (shape parameter for intensity) implying that spectral shape of ground motion records evidently have more disparity along the period axis than that of intensity. This is a desirable feature from our modeling point view, since it elucidates that PGA exercises more control on the peak intensity of ground motion response spectrum (as the spectral shape is anchored to PGA) than intensity of spectral shape itself. Compared to I, parameter S has the least variability manifesting that wideness of the spectral shape is well-bounded.

The major challenge that still remains for us is to find the correlation of these four dependent parameters (i.e., I, μ, $T_{sp,0}$, S) with respect to independent variables in best combination. For this purpose, best fit values of these four parameters are studied by partitioning them within magnitude, distance and V_{S30} bins.

Modeling Intensity of Spectral Shape

In order to find the best representative function for the intensity (I), spectral shapes of every major event are distributed into distance bins of 20 km (20 km range is selected to have enough of a number of data points in each bin to retain ample statistical meaning), and then mean values of peak spectral intensities are plotted against the mean values of distance for each bin. In this way, the approximate correlation between distance and intensity parameters is obtained. The best-fit is achieved by an exponential relation between intensity and distance as given by Equation 5. More importantly this functional form consistently remains similar for 16 major events investigated (see Table 1 for the list of major events, which are marked with an "a."

$$I(R) = a_{11}\mathrm{e}^{a_{22}R} \tag{5}$$

In Equation 5, a_{11} and a_{22} stand for the initial estimator coefficients, and essentially varying from one major event to another. In order to explore the magnitude dependence on intensity (I), estimator coefficients (i.e., a_{11} and a_{22}) computed for the 16 events are plotted against the magnitude of each major event. We found a relatively strong correlation between a_{11} and magnitude, whereas such a correlation did not exist for a_{22}. The resultant functional form for intensity therefore reads as:

$$I(M,R) = (a_1M + a_2)\mathrm{e}^{a_3R} \tag{6}$$

where (a_1M+a_2) now replaces the a_{11}, while a_3 remains equivalent of a_{22}. The same modeling approach is repeated for V_{S30} by examining the data within V_{S30} bins having intervals of 180 m/sec. The poor correlation obtained did not allow us using V_{S30} as an additional parameter to constrain for the intensity.

After constructing the equation form for I and integrating Equation 6 into Equation 4, Step 1 is repeated, thereby new statistical distributions of other parameters, namely μ, $T_{sp,0}$ and S are obtained. The similar updating procedure is iterated after constraining each functional form until the last form of equation is obtained for S. The reason for continuous data fitting as we progress in constraining and limiting the subfunctions is to find stable subfunctions and achieve the best unbiased estimator coefficients.

Modeling Predominant Period of Spectral Shape

There are two parameters μ and $T_{sp,0}$ set in Equation 4 to identify the location of peak intensity on the spectral axis (i.e., predominant period). These two parameters have concurrent effects on the resultant predominant period, while the former is more effective. Functional form for μ is therefore first explored. After casting equation form of μ, that of $T_{sp,0}$ is constrained to compensate for the residuals associated with μ. In fact, $T_{sp,0}$ inherently helps to reduce the overall misfit in predominant period prediction.

Unlike intensity function, we found strong correlation between predominant period and V_{S30} such that predominant period shifts to shorter period as V_{S30} increases (see Figure 5). Likewise, Figures 3 and 4 clearly show the magnitude and distance dependence on predominant period and consequently on μ and $T_{sp,0}$. The solution steps to find a suitable functional form for μ and $T_{sp,0}$ are similar to those described for I, and required several stages to adjust for distance, magnitude and V_{S30}. The final equation forms for μ and $T_{sp,0}$ yield

$$\mu(M,R,V_{S30}) = m_1R + m_2M + m_3V_{S30} + m_4 \tag{7}$$

$$T_{spec,0}(M,R) = t_1R + t_2M + t_3V_{S30} + t_4 \tag{8}$$

Note that both μ and $T_{sp,0}$ are simulated as linear function of magnitude, distance and V_{S30}. In Equations 7 and 8, m_1 to m_4 and t_1 to t_4 are the best estimator coefficients. Equations 7 and 8 are integrated in Equation 4 sequentially. First Equation 7 is implemented and nonlinear fit to spectral shape of each record is repeated and PDF of estimator coefficients in Equation 7 are obtained. After taking mean values of each estimator coefficient and constraining the Equation 7 in Equation 4, Equation 8 is next plugged into Equation 4 and similar process is repeated until the best estimator coefficients for Equation 8 are computed.

Modeling Wideness of Spectral Shape

Wideness of spectral shape describes its relative energy content. In other words, compared to narrow spectral peak, wide-band peak implies more distributed energy for a wide range of spectral periods. Originally in Equation 4, wideness of spectral shape is described by the parameter S, and its correlation against the independent parameters is examined using the same approach applied to other shape parameters. Among three independent parameters, magnitude and distance are well correlated with the wideness, and the following first-order equation reasonably represents their dependences and associated variability:

$$S(M,R) = s_1 R - (s_2 M + s_3) \tag{9}$$

This relation indicates that as magnitude increases, there is a corresponding increase in wideness of spectral shape with reduction in $S(M,R)$ (note that S is in the denominator in Equation 4). Unlike magnitude, distance has an opposite impact—spectral shape shows a tendency to being narrower as the distance from the source increases. Although there may be some correlation between V_{S30} and S, scarcity of data did not provide us any visible relation, thus functional form of S is kept limited to magnitude and distance only. Note that s_1, s_2 and s_3 are again the estimator coefficients, and they are computed using the process described for I, μ and $T_{sp,0}$.

Step 3: Finalizing the Model for Spectral Shape

It is worth re-emphasizing that because large variability of parameters following the Step 1 cannot be modeled in a single stage, in finalizing each subfunction, each equation is first constrained and then embedded into Equation 4. The updated approximation function is refitted to spectral data and new distributions of remaining unconstrained shape parameters are obtained. The same process is repeated to achieve the best estimator coefficients with minimal standard error. Our final model is shown in Figure 9. It should be noted that PGA is not included yet, and estimations are limited to spectral shape only. In order to predict the response spectrum ordinates, level of PGA is needed to scale (intensity-wise) the predicted spectral shape.

ATTENUATION MODEL FOR RESPONSE SPECTRAL ORDINATES

As shown in Figure 9, our model for response spectral attenuation is composed of two separate modules. The first module is for spectral shape prediction, and the second one is for PGA scaling (see Figure 10 for the GK07-PGA attenuation relation). Thus, final spectral ordinates are computed by anchoring the spectral shape to PGA as

$$\ln(SA) = [\ln(PGA) + \ln(SA_{norm})] + \sigma_{In(SA)} \tag{10}$$

where $\sigma_{ln(SA)}$ is the total standard error of response spectral attenuation relation. It should be emphasized that in order to reach the best prediction of response spectrum, both spectral shape model and PGA attenuation relation (in case if real PGA is not used) should concurrently provide robust estimates.

Robustness of the spectral shape model can be assessed by investigating how well the predominant period, peak spectral acceleration, and wideness of spectrum are simulated. While the third shape parameter requires visual interpretation, the first two can be quantified without ambiguity. Hence, they may serve as appropriate candidates for numerically testing the predictive power of our model and its estimator coefficients. Figure 11 compares the predicted and computed peak spectral acceleration and predominant period. Actual PGA values from all records are employed to scale the predicted spectral shape. Note that diagonal dash lines indicate the ideal one-to-one relation. It is evident from narrow band scattering of data along the diagonal that the peak spectral acceleration values are predicted in confidence using the spectral shape model when actual PGA values are used for scaling (Figure 11a). The data shows more scatter when plotted for

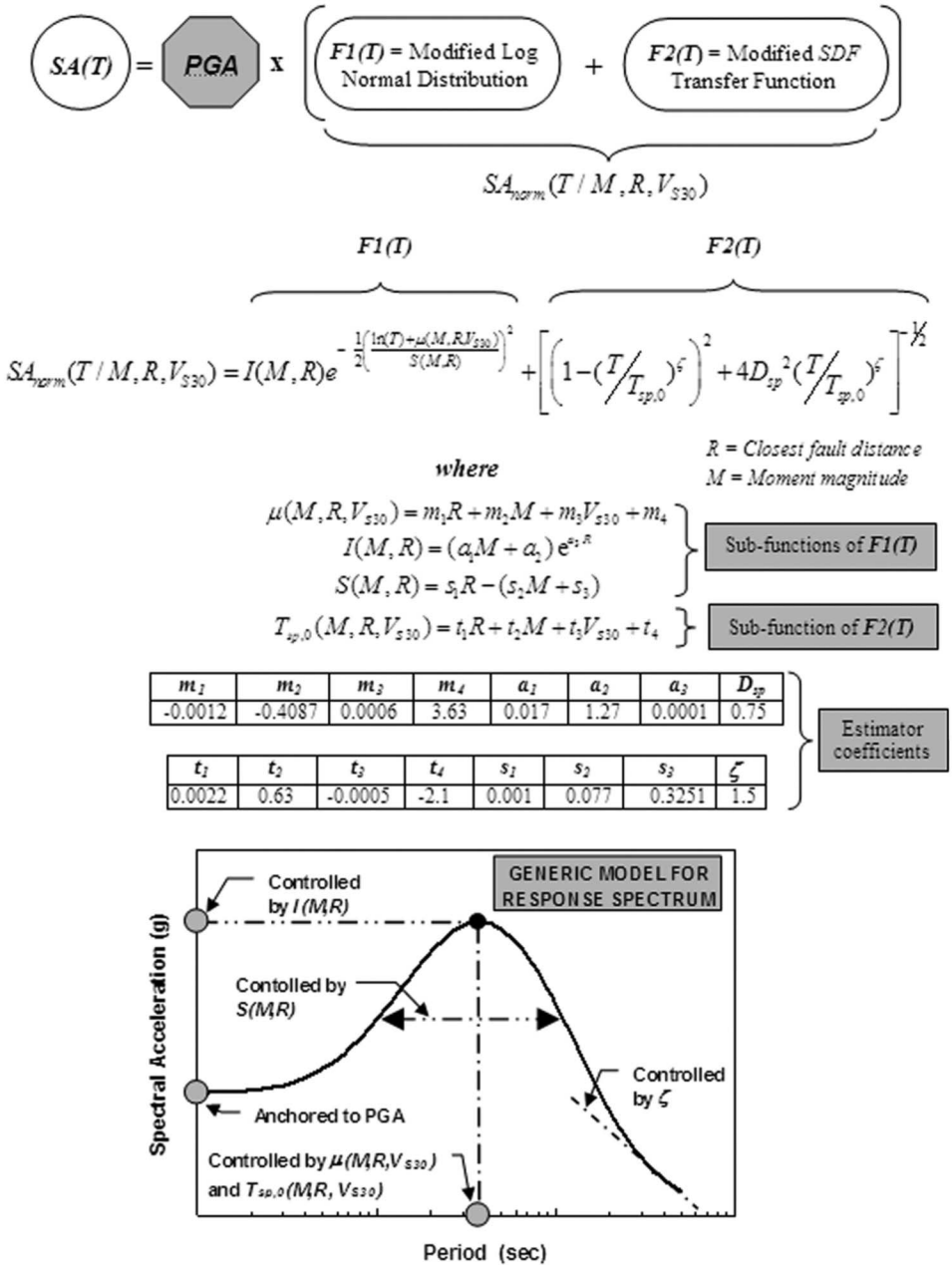

m_1	m_2	m_3	m_4	a_1	a_2	a_3	D_{sp}
-0.0012	-0.4087	0.0006	3.63	0.017	1.27	0.0001	0.75

t_1	t_2	t_3	t_4	s_1	s_2	s_3	ζ
0.0022	0.63	-0.0005	-2.1	0.001	0.077	0.3251	1.5

Figure 9. Graizer-Kalkan prediction model for 5% damped response spectral acceleration ordinates based on PGA attenuation relation.

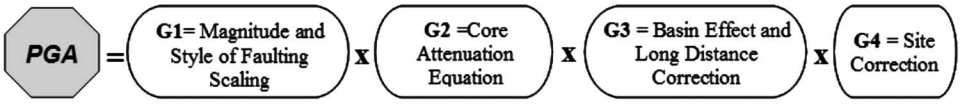

$$ln(Y) = \overbrace{ln[A(M,F)]}^{G1} - \overbrace{0.5ln[(1-r_0)^2 + 4D_0^2 r_0]}^{G2} - \overbrace{0.5ln[(1-\sqrt{r_1})^2 + 4D_1^2\sqrt{r_1}]}^{G3} + \overbrace{b_v ln(V_{S30}/VA)}^{G4} + \sigma_{lnY}$$

where

$$Y = PGA$$

$$r_0 = R/R_0 \qquad r_1 = R/R_1$$

$$A(M,F) = [c_1 \arctan(M + c_2) + c_3]\ F$$

$$R_0 = c_4 M + c_5$$

$$D_0 = c_6 \cos[c_7 (M + c_8)] + c_9$$

c_1	c_2	c_3	c_4	c_5	c_6	c_7	c_8	c_9	b_v	VA	R_1	σ_{lnY}
0.14	-6.25	0.37	2.237	-7.542	-0.125	1.19	-6.15	0.525	-0.24	484.5	100	0.552

Note (1): *To capture basin effect it is recommended to set $D_1 = 0.35$, otherwise $D_1 = 0.65$*
(2): *$F = 1.00$ for strike-slip and normal faulting; $F = 1.28$ for reverse faulting*
(3): *R = Closest fault distance and M = Moment magnitude*

Figure 10. GK07-PGA attenuation relation for free-field horizontal component of ground motion (Graizer and Kalkan 2007).

predominant period (Figure 11b), indicating that variability in estimation of this parameter is larger than the peak intensity. Unlike peak spectral acceleration, predominant period is a direct output of the spectral shape model meaning that it is not affected by the PGA scaling.

For completeness, Figure 12a compares the actual and predicted PGA values based on GK07-PGA attenuation relation, and Figure 12b shows one-to-one comparisons of peak spectral acceleration and its predicted values using the GK07-PGA attenuation relation. The power of prediction relies inherently on prediction of PGA; if PGA is predicted well, our prediction for the complete spectrum will be better.

The shape of final spectrum for various magnitude, distance, site condition, and style of faulting are demonstrated next in Figures 13 and 14. Figure 13a first exemplifies our predictions of median spectrum for firm soil (V_{S30}=270 m/sec) and rock site (V_{S30} =760 m/sec) conditions considering the effect of magnitude 7.5 earthquake at fault distances of 1, 10, 30, and 100 km. In Figure 13b, earthquake magnitude is varied (M5.5, 6.5, and 7.5), while the fault distance is kept constant at 10 km. Note that the GK07-PGA attenuation relation is used to construct the response spectra. Increase in magnitude and/or increase in distance shifts the predominant period of spectrum to larger values (spectral behavior controlled by μ and $T_{sp,0}$). Wider spectrum is generated by larger magnitudes implying that energy at different periods is enriched by the complex wave

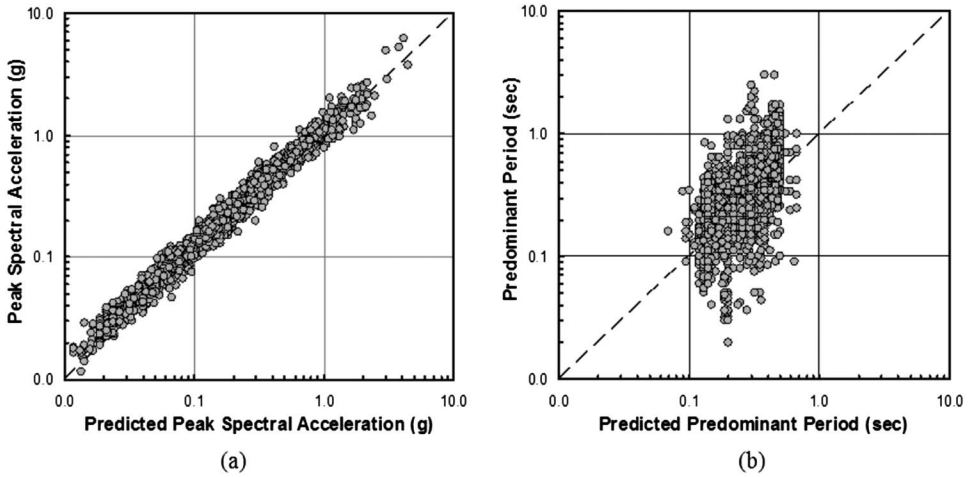

Figure 11. One-to-one comparison of (a) actual and predicted peak spectral acceleration; (b) actual and predicted predominant period (*in computation of peak spectral acceleration, actual PGA values are used for scaling spectral shapes*).

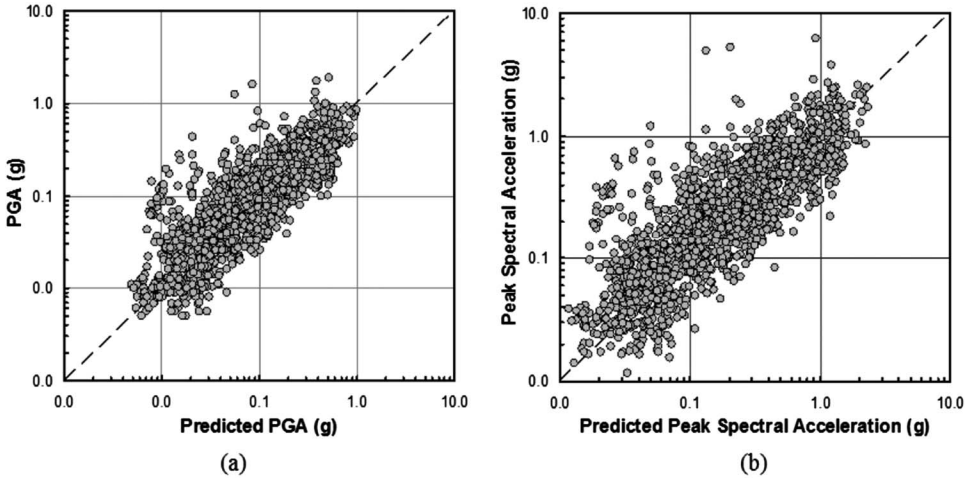

Figure 12. One-to-one comparison of (a) actual and predicted PGA based on GK07 PGA attenuation relation; (b) actual and predicted peak spectral acceleration (*in computation of peak spectral acceleration, predicted PGA values based on GK07 PGA attenuation relation are used for scaling spectral shapes*).

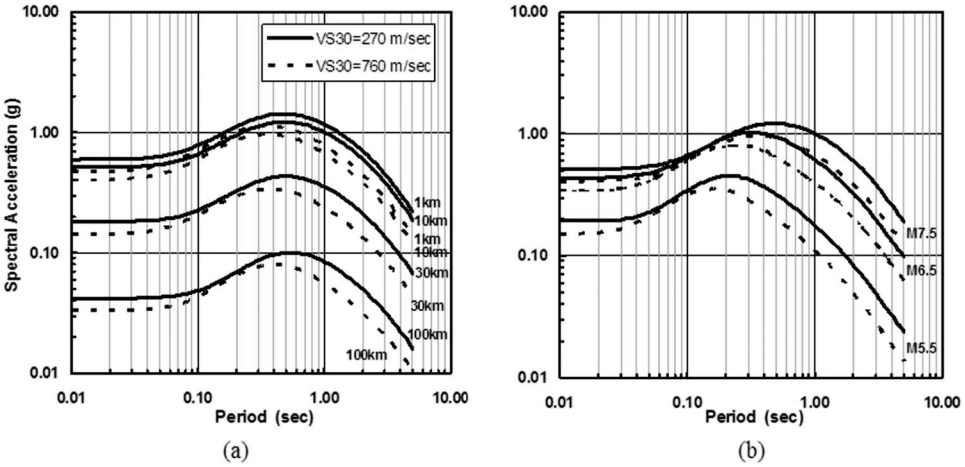

Figure 13. Prediction of response spectral ordinates based on integration of GK07 PGA attenuation relation with Graizer-Kalkan spectral shape predictive model for (a) M7.5 event with variable fault distances; (b) a constant fault distance of 10 km with variable magnitudes (*style of faulting=strike-slip*).

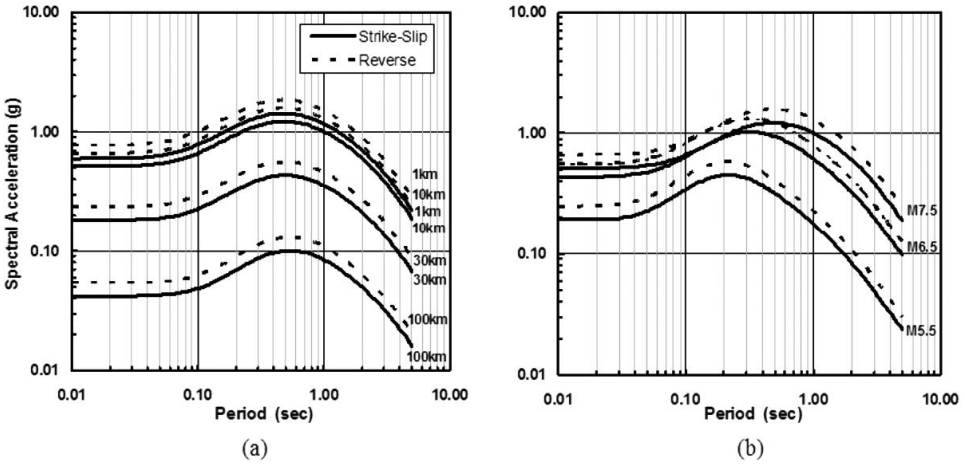

Figure 14. Prediction of response spectral ordinates based on integration of GK07 PGA attenuation relation with Graizer-Kalkan spectral shape predictive model for (a) M7.5 event with variable fault distances; (b) a constant fault distance of 10 km with variable magnitudes (V_{S30} =270 m/sec).

propagation from lengthy rupture plane. In contrast, small-magnitude events have the tendency of showing relatively narrower spectral shape whose peak is shifted toward shorter periods.

The effects of style of faulting are demonstrated next in Figure 14 considering similar distance and magnitude combinations. It is possible to observe that there is a constant difference over all periods between spectral plots (i.e., between dashed and continuous lines for each distance and/or magnitude levels). Reverse faulting results in a constant 28% amplification of spectral ordinates compared to strike-slip rupture. Although reverse faulting earthquake produces higher amplitudes of motion at short and intermediate periods than strike-slip events (Bommer et al. 2003), our spectral shape model has not incorporated period dependence of the focal mechanism, and consequently relies on PGA scaling in that sense. It is therefore the invariant difference between spectral plots stems from the GK07-PGA relation utilized. If one uses a PGA attenuation relation different from the GK07-PGA, the effects of style of faulting on spectral ordinates may be different.

STANDARD ERROR

The total standard error term of attenuation relations has always been a controversial parameter, since it is often open to misinterpretations. Lower standard error in prediction is a desirable attribute of the model and denotes the quality of overall fitting. This term can be expressed in general form as:

$$\sigma = \sqrt{\sum (x_i - x_i')^2/(n-p)} \tag{11}$$

where x_i denotes the i^{th} value of observation and x_i' is its prediction. $(x_i - x_i')$ is the residual of the i^{th} observation, and p is the number of dependent parameters of estimation. Equation 11 shows that when number of data points (n) increases, the standard error has the tendency to reduce provided that the predictive power of the model does not diminish. It is also a truism that associated prediction errors with low intensity records are much lower than those for high intensity records due to increased variability with amplification of intensity. It is therefore possible to reduce the total standard error of prediction by injecting low-intensity aftershock records into dataset (whereby contribution of square of residuals are less than the increase in number of points), and/or by eliminating the outliers associated with high intensity records (e.g., accelerograms from Tarzana station). In both conditions, total standard error of predictions may be artificially reduced. In this study, neither low-intensity aftershock records were included in our database, nor were the outliers from the main shocks eliminated.

It should be also emphasized that final parameters of our model are valid for a magnitude range of $4.9 < M < 7.9$ and a distance range up to 200 km (although we utilized data beyond that due to their relatively smaller weight, we recommend that our ground motion prediction model should be used up to 200 km—a distance limit sufficient for most engineering applications).

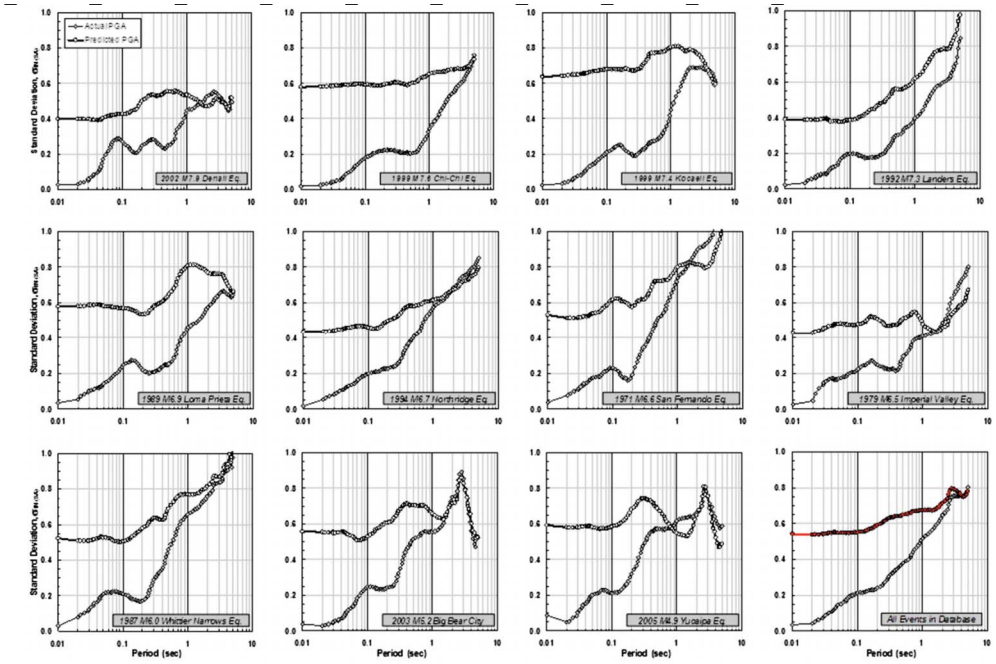

Figure 15. Standard deviation of spectral acceleration ($\sigma_{\ln(SA)}$) computed for major events (*predicted spectral shapes are anchored to actual and predicted PGAs separately; PGA predictions are based on GK07-PGA attenuation relation*).

Prior to addressing the total standard error of our model and its spectral period variations, it is instructive to explore the standard error corresponding to each major event separately. Figure 15 displays the segregation of the total standard error for 11 events, thus the quality of fit can be assessed effectively at the earthquake level. Two different plots for each event correspond to standard error when the actual PGA of records is used or the GK07-PGA attenuation is utilized for scaling. The plot that converges to zero standard error at $T=0$ corresponds to the spectral error based on real PGA. Both error distributions show a tendency toward increasing with increase in period, a common feature of all attenuation relations of response spectral ordinates. The possible explanation for this behavior is the enhanced variability of spectral acceleration at long periods due to a number of different physical phenomena including, for example, basin effect. Even exact scaling of spectral shape to real PGA of accelerograms does not noticeably alleviate reduction of the standard error for some events after 1.0 sec and for some others beyond 2.0 sec. In general, both standard error plots merge at long periods. In rare cases (e.g., Denali for $2.0<T<3.0$ sec), error in prediction using GK07-PGA attenuation compensates the error in prediction of spectral shape and results in better estimates of response spectrum than the case when real PGA is utilized. At short periods, when the GK07-PGA attenuation is used, total standard error ($\sigma_{ln(SA)}$) becomes closer to the

GK07-PGA attenuation relation's original standard error ($\sigma_{ln(Y)}$) of 0.552, since GK07-PGA attenuation expression was essentially derived using the same database with additional PGA entities.

The final plot shown in Figure 15 (right lower corner) depicts the total standard error ($\sigma_{ln(SA)}$) when all the data is accounted for. The numerical values of $\sigma_{ln(SA)}$ at each spectral period are tabulated in Table 2. Note that standard errors corresponding to the real PGA are actually the exact standard errors of our spectral shape model since it is developed independently from PGA. If the predicted PGA values are used in lieu of the exact PGA, then the standard error in PGA attenuation relation used inherently propagates into the predicted response spectrum. When the GK07-PGA attenuation is used for anchoring the spectral shapes, the standard error ($\sigma_{ln(SA)^b}$ as shown in Table 2) starts from 0.544 at 0.01 sec and reaches 0.781 at 5.0 sec. This range of total standard errors is comparable to the recent NGA relations.

Note that although we used the GK07-PGA model in the quantitative analysis, the resulting model for response spectral shape can be used with any other modern attenuation relation. To facilitate this, a correlation function between two standard errors is computed to get the final standard error of response spectral ordinates ($\sigma_{\ln SA}$) as:

$$\sigma_{lnSA} = \sigma_{PGA} \frac{\sigma_{Spectral\text{-}shape}}{0.092 \ln(T) + 0.404} \tag{12}$$

where σ_{PGA} is the standard error of the PGA attenuation relation to be used. $\sigma_{Spectral\text{-}shape}$ are tabulated in Table 2 under the column $\sigma_{ln(SA)^a}$.

In order to investigate whether our predictions are biased against any independent parameters of estimations, residual plots of 0.1, 0.3 and 1.0 sec spectral acceleration estimates for the full data set as functions of magnitude, fault distance, and V_{S30} are plotted in Figure 16. With respect to three independent variables, no significant trends are observed especially at short periods while slight variations are visible for 1.0 sec.

SUMMARY AND FINAL REMARKS

This paper, a sequel to our earlier work on PGA attenuation relation development, presents a new attenuation relation for the 5% damped pseudospectral acceleration ordinates of free-field horizontal component of ground motion from shallow-crustal earthquakes. Compared to the existing models, an original feature of the model is its new functional form developed specifically for ground motion spectral shape (i.e., spectrum normalized by PGA). Hence, the spectral response ordinates are computed by anchoring the predicted spectral shape to PGA, which can be either an actual measured value or a predicted one by any appropriate PGA attenuation relation preferred. Unlike classical spectral attenuation relations, which constitute a discrete set of estimator coefficients for each spectral period, the proposed model is designed as a continuous function of period. Thus, the classical long set of estimator coefficients is replaced with a few controlling parameters.

Table 2. Standard deviations for spectral shape[a] and response spectral acceleration ordinates[b] (spectral shape=$SA(T)/PGA$, where T=Period)

Period (sec)	$\sigma_{\ln(SA)}$[a]	$\sigma_{\ln(SA)}$[b]	Period (sec)	$\sigma_{\ln(SA)}$[a]	$\sigma_{\ln(SA)}$[b]	Period (sec)	$\sigma_{\ln(SA)}$[a]	$\sigma_{\ln(SA)}$[b]
PGA	—	0.552	0.140	0.223	0.563	0.800	0.467	0.672
0.010	0.036	0.544	0.150	0.226	0.567	0.850	0.477	0.671
0.020	0.044	0.540	0.160	0.230	0.571	0.900	0.491	0.672
0.022	0.053	0.540	0.170	0.230	0.575	0.950	0.506	0.675
0.025	0.063	0.541	0.180	0.231	0.579	1.000	0.519	0.675
0.029	0.073	0.542	0.190	0.236	0.585	1.100	0.531	0.675
0.030	0.081	0.543	0.200	0.242	0.591	1.200	0.542	0.676
0.032	0.088	0.544	0.220	0.249	0.597	1.300	0.553	0.675
0.035	0.096	0.546	0.240	0.257	0.603	1.400	0.564	0.675
0.036	0.102	0.547	0.250	0.266	0.609	1.500	0.577	0.676
0.040	0.108	0.549	0.260	0.275	0.615	1.600	0.591	0.683
0.042	0.114	0.550	0.280	0.286	0.621	1.700	0.602	0.687
0.044	0.119	0.551	0.290	0.296	0.626	1.800	0.615	0.695
0.045	0.125	0.551	0.300	0.305	0.630	1.900	0.631	0.705
0.046	0.132	0.550	0.320	0.314	0.633	2.000	0.646	0.715
0.048	0.139	0.549	0.340	0.323	0.636	2.200	0.661	0.726
0.050	0.145	0.549	0.350	0.328	0.637	2.400	0.679	0.740
0.055	0.152	0.549	0.360	0.334	0.638	2.500	0.704	0.764
0.060	0.160	0.549	0.380	0.342	0.640	2.600	0.728	0.783
0.065	0.167	0.548	0.400	0.348	0.641	2.800	0.749	0.796
0.067	0.176	0.547	0.420	0.353	0.641	3.000	0.754	0.794
0.070	0.184	0.547	0.440	0.359	0.641	3.200	0.754	0.788
0.075	0.192	0.548	0.450	0.365	0.643	3.400	0.753	0.781
0.080	0.198	0.549	0.460	0.370	0.645	3.500	0.754	0.776
0.085	0.202	0.549	0.480	0.376	0.648	3.600	0.756	0.771
0.090	0.205	0.550	0.500	0.383	0.651	3.800	0.759	0.769
0.095	0.209	0.550	0.550	0.391	0.653	4.000	0.755	0.759
0.100	0.212	0.551	0.600	0.401	0.656	4.200	0.751	0.750
0.110	0.216	0.553	0.650	0.413	0.659	4.400	0.758	0.753
0.120	0.217	0.555	0.667	0.426	0.662	4.600	0.765	0.758
0.130	0.219	0.557	0.700	0.441	0.667	4.800	0.779	0.765
0.133	0.221	0.560	0.750	0.454	0.670	5.000	0.801	0.781

[a] Standard error for spectral shape. (They should be used when the predicted spectral shape is anchored to actual PGA)

[b] Standard errors when the Graizer and Kalkan (2007) attenuation relation for PGA is used to predict response spectrum

We used nonlinear optimization and sequential subfunction constraining to adequately capture the spectral shape characteristics. This technique eliminates the independent regressions repeated at each spectral period as in the conventional approach and

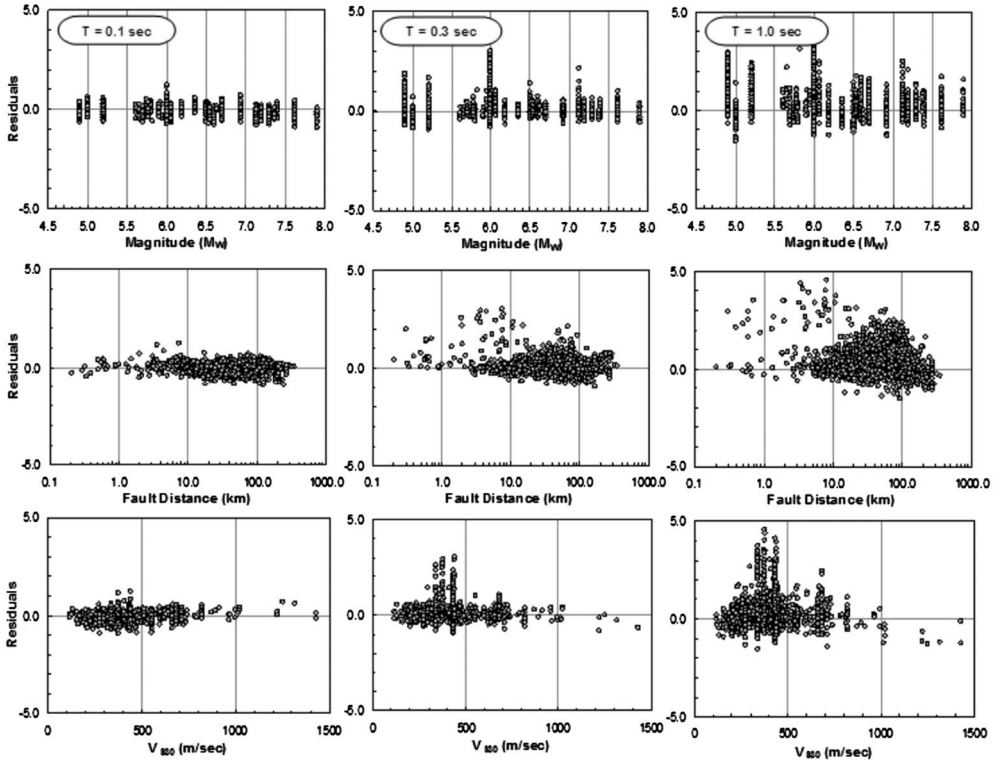

Figure 16. Distribution of residuals of spectral shape at spectral period, T=0.1, 0.3 and 1.0 sec with respect to magnitude, closest distance and V_{S30}.

directly provides smoothed spectral shapes. PDF of each estimator coefficient within each spectral shape function is obtained by consecutively fitting an approximation function to spectrum of each record.

The predictive model for spectral shape is structured on the main shocks in the NGA database with a number of additions. The formal model to predict the response spectrum based on the GK07-PGA attenuation relation is robust and practically yields good predictive performance against the actual spectral data in a range of magnitudes from 4.9 to 7.9 within a range of distances from 0 to 200 km, and for various site conditions. The spectral shape model utilizes earthquake magnitude, fault distance and V_{S30} measurement as the independent parameters of predictions. Other source parameters that cannot be defined with confidence in advance (e.g., depth to the surface of the rupture, hanging wall) were intentionally excluded. Formulation of response spectrum by a continuous function of period allows calculation of its ordinates at any period of interest within the model range. Although the stability of spectral shape up to 10 sec was verified through numerous testing, the model range was set to 0.01 to 5.0 sec, because 5.0 sec is the cutoff for the long-period filter in majority of the records employed.

Our predictive model uses linear site correction to modify the shape with respect to V_{S30} classification. This correction shifts the bump in the response spectrum to longer periods as the V_{S30} decreases without changing intensity or wideness of spectral shape function. Another correction associated with V_{S30} stems from the PGA attenuation used. The GK07-PGA attenuation relation adapts linear site amplification based on V_{S30} to correct for the near-surface site conditions, therefore the total site correction on the response spectrum has two sources: (i) spectral shape model differentiates the location of spectral peak; (ii) GK07-PGA attenuation relation makes adjustment on the intensity according to change in V_{S30}. The formal spectral acceleration attenuation model was tested and is recommended for use in the range of $200 < V_{S30} < 1200$ m/sec.

Basin effect was incorporated into the GK07-PGA attenuation model by amplifying (relatively to the nonbasin sites) ground motion at distances of more than 30 to 50 km when deep sedimentary basin is present. Since the spectral shape is anchored to the PGA, there are period-independent basin influences on the predicted response spectrum. The same applies for focal mechanism. When the GK07-PGA attenuation is used, the spectrum for reverse faulting is 28% larger than that of strike-slip fault. This difference remains the same along the spectral period axis.

The combined attenuation model of PGA and response spectra presented in this paper is controlled by a number of measurable earthquake and site condition parameters and represents a complete ground motion prediction model. The modeling approach developed can be potentially used for earthquakes in other seismotectonic regions with subduction and intraplate events. The proposed model provides significant ease in both implementation and interpretation of its simplistic equation form as well as controlling physical parameters, while providing comparable standard error to those of the recent NGA relations. Comparisons of our model with the NGA relations based on recorded data and seismic hazard mapping results for California are currently underway. We expect our approach to ground motion attenuation modeling to be evolving in the future based on additional data recorded in the near-field by high-resolution digital instruments especially from large ($M \sim 8.0$) earthquakes.

ACKNOWLEDGMENTS

We thank the Pacific Earthquake Engineering Research Center for providing access to the NGA database. Sincere thanks are extended to Drs. Polat Gülkan, Kenneth Campbell, Walter Silva, Mihailo Trifunac, and two anonymous reviewers whose comments and suggestions improved the technical quality of the paper. Any opinions, findings, and conclusions or recommendations expressed in this paper are those of the authors solely and do not necessarily reflect the views of the Federal government or the California State government.

The attenuation model presented in this paper was implemented in both FORTRAN and MATLAB, and their source codes are available upon request.

REFERENCES

Abrahamson, N. A., and Silva, W. J., 1997. Empirical response spectral attenuation relations for shallow crustal earthquakes, *Seismol. Res. Lett.* **68**, 94–127.

Abrahamson, N. A., and Silva, W. J., 2008. Summary of the Abrahamson and Silva NGA ground motion relations, *Earthquake Spectra* **24**, 67–98.

Ambraseys, N. N., Simpson, K. A., and Bommer, J. J., 1996. Prediction of horizontal response spectra in Europe, *Earthquake Eng. Struct. Dyn.* **25**, 371–400.

Bakir, S., Sucuoglu, H., and Yilmaz, T., 2002. An overview of local site effects and the associated building damage in Adapazari during the 17 August 1999 Izmit earthquake, *Bull. Seismol. Soc. Am.* **92**, 509–526.

Biot, M. A., 1933. Theory of elastic systems vibrating under transient impulse with application to earthquake proof buildings, *Proc. Natl. Acad. Sci. U.S.A.* **19**, 262–268.

Bommer, J. J., Douglas, J., and Strasser, F. O., 2003. Style-of-faulting in ground-motion prediction equations, *Bull. Earthquake Eng.* **1**, 171–203.

Boore, D. M., Joyner, W. B., and Fumal, T. E., 1997. Equations for estimating horizontal response spectra and peak acceleration from western North American earthquakes: a summary of recent work, *Seismol. Res. Lett.* **68**, 128–153.

Boore, D. M., and Atkinson, G. M., 2008. Ground-motion prediction equations for the average horizontal component of PGA, PGV, and 5%-damped PSA at spectral periods between 0.01 s and 10.0 s, *Earthquake Spectra* **24**, 99–138.

Campbell, K. W., 1997. Empirical near-source attenuation relationships for horizontal and vertical components of peak ground acceleration, peak ground velocity, and pseudo-absolute acceleration response spectra, *Seismol. Res. Lett.* **68**, 154–179.

Campbell, K. W., and Bozorgnia, Y., 2008. NGA ground motion model for the geometric mean horizontal component of PGA, PGV, PGD and 5% damped linear elastic response spectra for periods ranging from 0.01 to 10 s, *Earthquake Spectra* **24**, 139–172.

Chiou, B., and Youngs, R., 2008. An NGA model for the average horizontal component of peak ground motion and response spectra, *Earthquake Spectra* **24**, 173–216.

Douglas, J., 2001. *A comprehensive worldwide summary of strong-motion attenuation relationships for peak ground acceleration and spectral ordinates (1969 to 2000)*, Imperial College of Science, Technology and Medicine Department of Civil & Environmental Engineering London, U. K. Dept. Report, Jan.

Douglas, J., 2002. Errata of and additions to ESEE Report No. 01-1: 'A comprehensive worldwide summary of strong-motion attenuation relationships for peak ground acceleration and spectral ordinates (1969 to 2000), Imperial College of Science, Technology and Medicine Department of Civil & Environmental Engineering London, U. K. Dept. Report, Oct.

Field, E. H., 2000. A modified ground-motion attenuation relationship for Southern California that accounts for detailed site classification and a basin-depth effect, *Bull. Seismol. Soc. Am.* **90**, 209–221.

Frankel, A., Carver, D., Cranswick, E., Bice, T., Sell, R., and Hanson, S., 2001. Observation of basin ground motions from a dense seismic array in San Jose, California, *Bull. Seismol. Soc. Am.* **91**, 1–12.

Fukushima, Y., Berge-Thierry, C., Volant, P., Griot-Pommera, D. A., and Cotton, F., 2003. Attenuation relation for West Eurasia determined with recent near-fault records from California, Japan and Turkey, *J. Earthquake Eng.* **7**, 1–26.

Graizer, V., Shakal, A., Scrivner, C., Hauksson, E., Polet, J., and Jones, L., 2002. TriNet strong-motion data from the M 7.1 Hector Mine, California, earthquake of 16 October 1999, *Bull. Seismol. Soc. Am.* **92**, 1525–1541.

Graizer, V., and Kalkan, E., 2007. Ground motion attenuation model for peak horizontal acceleration from shallow crustal earthquakes, *Earthquake Spectra* **23**, 585–613.

Gülkan, P., and Kalkan, E., 2002. Attenuation modeling of recent earthquakes in Turkey, *J. Seismol.* **6**, 397–409.

Housner, G. W., 1959. Behavior of structures during earthquakes, *J. Engrg. Mech. Div.* **85**, 109–129.

Idriss, I. M., 2008, An NGA empirical model for estimating the horizontal spectral values generated by shallow crustal earthquakes, *Earthquake Spectra* **24**, 217–242.

Joyner, W. B., 2000. Strong motion from surface waves in deep sedimentary basins, *Bull. Seismol. Soc. Am.* **90**, 95–112.

Kalkan, E., and Gülkan, P., 2004a. Empirical attenuation equations for vertical ground motion in Turkey, *Earthquake Spectra* **20**, 853–882.

——, 2004b. Site-dependent spectra derived from ground motion records in Turkey, *Earthquake Spectra* **20**, 1111–1138.

Kanno, T., Narita, A., Morikawa, N., Fujiwara, H., and Fukushima, Y., 2006. A new attenuation relation for strong ground motion in Japan based on recorded data, *Bull. Seismol. Soc. Am.* **96**, 879–897.

Lee, V. W., Trifunac, M. D., Todorovska, M. I., and Novikova, E. I., 1995. *Empirical equations describing attenuation of peak of strong ground motion, in terms of magnitude, distance, path effects and site conditions*, *Report No. CE 95-02*, Los Angeles, California. 268 pp.

Mori, J., Kanamori, H., Davis, J., Hauksson, E., Clayton, R., Heaton, T., Jones, L., and Shakal, A., 1999. Major improvements in progress for southern California earthquake monitoring, *EOS, Transactions, American Geophysical Union* **79**, 217–221.

Newmark, N. M., Blume, J. A., and Kapur, K. K., 1973. Seismic design criteria for nuclear power plants, *J. Power Div.* **99**, 287–303.

Power, M., Chiou, B., Abrahamson, N., and Roblee, C., 2006. The next generation of ground motion attenuation models (NGA) project: An overview, in *Proceedings, Eighth National Conference on Earthquake Engineering*, Paper No. 2022.

Rowshandel, B., 2006. Incorporating source rupture characteristics into ground-motion hazard analysis models, *Seismol. Res. Lett.* **77**, 708–722.

Sabetta, F., and Pugliese, A., 1996. Estimation of response spectra and simulation of nonstationary earthquake ground motions, *Bull. Seismol. Soc. Am.* **86**, No. 2, 337–352.

Sadigh, K., Chang, C.-Y., Egan, J. A., Makdisi, F., and Youngs, R. R., 1997. Attenuation relationships for shallow crustal earthquakes based on California strong motion data, *Seismol. Res. Lett.* **68**, 180–189.

Safak, E., Erdik, M., Beyen, K., Carver, D., Cranswick, E., Celebi, M., Durukal, E., Ellsworth, W., Holzer, T., Meremonte, M., Mueller, C., Ozel, O., and Toprak, S., 2000. Kocaeli, Turkey,

Earthquake of August 17, 1999: Reconnaissance report, Ch. 5—Recorded mainshock and aftershock motions, *Earthquake Spectra* **16**, 97–112.

Silva, W. J., Youngs, R. R., and Idriss, I. M., 2001. Development of design response spectral shapes for Central and Eastern U. S. (CEUS) and Western U. S. (WUS) rock site conditions, in *Proceedings of the Organization for Economic Coordination and Development of the Nuclear Energy Agency (OECE-NEA) Workshop on Engineering Characterization of Seismic Input, Nov. 15–17, 1999 NEA/CSNI/R(2000) 2*, 185–268.

Somerville, P., Smith, N. F., Graves, R. W., and Abrahamson, N., 1997. Modification of empirical strong ground motion attenuation relations to include the amplitude and duration effects of rupture directivity, *Seismol. Res. Lett.* **68**, 199–222.

Theodulidis, N. P., and Papazachos, B. C., 1994. Dependence of strong ground motion on magnitude-distance, site geology and macroseismic intensity for shallow earthquake in Greece: II horizontal psedovelocity, *Soil Dyn. Earthquake Eng.* **13**, 317–343.

Udwadia, F. E., and Trifunac, M. D., 1973. Damped Fourier spectrum and response spectra, *Bull. Seismol. Soc. Am.* **63**, 1775–1783.

Wald, D. J., Quitoriano, V., Heaton, T. H., and Kanamori, H., 1999a. Relationships between peak ground acceleration, peak ground velocity and modified Mercalli intensity in California, *Earthquake Spectra* **15**, 557–564.

Wald, D. J., Quitoriano, V., Heaton, T. H., Kanamori, H., Scrivner, C. W., and Worden, C. B., 1999b. TriNet ShakeMaps: rapid generation of instrumental ground motion and intensity maps for earthquakes in Southern California, *Earthquake Spectra* **15**, 537–556.

Wilson, H. B., Turcotte, H. L., and Halpern, D., 2003. *Advanced Mathematics and Mechanics Applications Using MATLAB*, 3rd edition, Chapman & Hall/CRC, Boca Raton, 696 pp.

(Received 26 July 2007; accepted 19 September 2008)